Aalborg Universitet

AALBORG UNIVERSITY

DENMARK

Finite Control Set Model Predictive Control for LCL-Filtered Grid-Tied Inverter with Minimum Sensors

Chen, Xiaotao; Wu, Weimin; Gao, Ning; Chung, Henry; Liserre, Marco; Blaabjerg, Frede

Finite Control Set Model Predictive Control for LCL-Filtered Grid-Tied Inverter with Minimum Sensors

Xiaotao Chen, Weimin Wu, *Member, IEEE*, Ning Gao, Henry Shu-Hung Chung, *Fellow, IEEE*, Marco Liserre, *Fellow, IEEE*, and Frede Blaabjerg, *Fellow, IEEE*

Abstract—**Recently, Finite Control Set Model Predictive Control (FCS-MPC) has been successfully applied in the grid-tied inverter with LCL filter. However, to achieve active damping and grid synchronization, many sensors are required, increasing cost and complexity. In addition, a considerable computational delay should be addressed when it is experimentally implemented, which may degrade the performance of overall system. In order to reduce the number of sensors, eliminate the computational delay, and enhance the control reliability of system, a novel FCS-MPC strategy with merely grid-injected current sensors is proposed, which contains four compositions: virtual flux observer, state observer, delay compensation and FCS-MPC algorithm based on estimations. A 3-kW/3-phase/110V experimental platform is established to validate that utilizing the proposed observations-based control method with only grid-injected current sensors is capable to obtain satisfactory performance of grid synchronization and high quality grid-injected current both under balanced and unbalanced grid voltage condition.**

Index Terms—**Control reliability, delay compensation, FCS-MPC, grid synchronization, LCL filter, state observer, virtual flux observer.**

I. Introduction

AS interfaces between DC sources and grids, grid-tied inverters are core components of distributed generation systems, like roof-top photovoltaics [1]-[3]. In order to achieve great performance of them, besides the classical linear control strategies [4], [5], a large amount of nonlinear control schemes, such as sliding mode control (SMC), passivity-based control (PBC) [6], [7] and so on, have been proposed. As one of the nonlinear control schemes, model predictive control (MPC) has also attracted many attentions in recent years, since the problem of computational burden has been preliminary solved [8]-[10].

Generally, MPC can be classified into two categories: Continuous Control Set Model Predictive Control (CCS-MPC) and Finite Control Set Model Predictive Control (FCS-MPC), depending on how the switching signals that control the operation of grid-tied inverter are generated [11], [12]. For CCS-MPC, the control scheme yields a continuous output which is needed to be processed by a modulator to obtain the gate signals [13]. For FCS-MPC, it does not adopt a modulation stage but relies on a finite number of output states of inverters, which is employed to evaluate the cost function [14]. In contrast to CCS-MPC, FCS-MPC is the best known due to the technique advantages include: straightforward handling of nonlinearities and constraints, good dynamic response, and simple implementation [15]-[17].

Recently, FCS-MPC strategy was proposed for the LCL-filtered grid-tied inverter [11], where it requires two kinds of current sensors and two types of voltage sensors, increasing the cost and complexity. In order to reduce the number of sensors for measuring the state variables [18]-[23] and the grid voltage [24]-[27], many control methods with fewer sensors had been utilized, respectively.

An approach, which decreases the sensors of state variables, was described in [18], where the capacitor current loop was merged with the grid-injected current loop by transforming the block diagram. However, it saves only two capacitor current sensors. For further sensors saving, the state observer [19], [20] and Kalman filter (KF) [21], [22] based on state-space model were investigated, which were both utilized to estimate the state variables of filter via the closed-loop system. Compared with the state observer, the issues of higher computational burden and more complex parameter adjustment process are existed for KF [23]. Therefore, the state observer is adopted for estimating the all three state variables in this paper. Although the total number of current sensors can be reduced by adopting the state observer, the grid voltage still needs to be measured, which leads to an extra sensor.

Many grid voltage sensorless schemes have been reported in the literature [24], [25], where the concept of virtual flux (VF) is well-known, and it has been universally investigated. However, due to problems of DC drift and initial bias caused by pure integrator, some necessary solutions for addressing these

X. Chen, W. Wu and N. Gao are with the Electrical Engineering Department, Shanghai Maritime University, Shanghai 201306, China (e-mail: 18201806089@163.com; wmwu@shmtu.edu.cn; ngao@shmtu.edu.cn).

H.S.-H. Chung is with the Electronic Engineering Department, City University of Hong Kong, Kowloon, Hong Kong, SAR (e-mail: eeshc@cityu.edu.hk).

M. Liserre is with Christian-Albrechts University of Kiel, 24118 Kiel, Germany (e-mail: liserre@ieee.org).

F. Blaabjerg is with the Energy Engineering Department, Aalborg University, Aalborg 9100, Denmark (e-mail: fbl@et.aau.dk).

issues are required. A first order low pass filter (LPF) is generally used owing to its simple implementation, and the magnitude and phase errors introduced by this filter can be handled by a compensation gain [26]. For enhancing the VF performance, many complex solutions were proposed, e.g. reference [27] utilizes a virtual flux observer with negative feedback resonant filter and a delay compensation algorithm to alleviate the steady-state error and the delay. However, although these strategies offer a better performance, the complexity of algorithms should be taken into account.

In this paper, a novel observations-based FCS-MPC strategy for LCL-filtered grid-tied inverter is proposed using only grid-injected current sensors. The control method is based on all four observations instead of measurements, where inverter-side current, capacitor voltage and grid-injected current are estimated via state observer. For the grid voltage, a VF-based grid voltage sequence extraction strategy is adopted to separate the positive- and negative- sequence components, so that the satisfactory performance of grid-injected current is obtained under unbalanced grid voltage condition. The performance of the control strategy is verified by theoretical analysis and experimental tests. The rest of this paper is organized as follows. The conventional FCS-MPC strategy for LCL filtered grid-tied inverter is first presented in Section II. Then, the proposed FCS-MPC method with full status estimations based on virtual flux and state observer is described in Section III. Next, experimental results are documented in Section IV, where the performance of grid synchronization and the high quality grid-injected current both under balanced and unbalanced grid voltage condition are analyzed. Finally, conclusions are drawn in Section V.

II. CONVENTIONAL FCS-MPC STRATEGY FOR LCL-FILTER-BASED GRID-TIED INVERTER
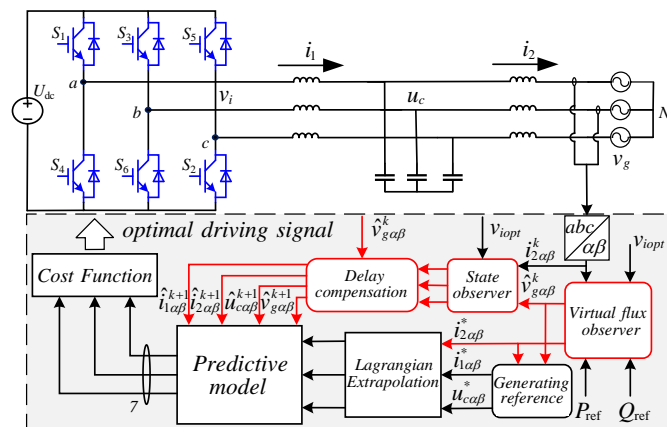
A. Grid-Connected Inverter Model

Fig. 1 Proposed FCS-MPC strategy for grid-tied inverter with LCL filter.

The structure of three phase grid-tied inverter with LCL filter is depicted in Fig. 1. As shown in Fig. 1, U_{dc}, v_i, u_c and v_g represent the DC bus voltage, the inverter output voltage, the capacitor voltage and the grid voltage, respectively. i_1 and i_2 denote the inverter-side current and the grid-injected current respectively. The inverter output voltage is combined by eight

switching states and it can be described as a complex space vector in αβ stationary coordinate system,

$$v_{i\alpha\beta}(n) = \begin{cases} "0", & n = \{0,7\} \\ \dfrac{2}{3}U_{dc}e^{j\frac{\pi}{3}(n-1)}, & n = \{1,2...,6\} \end{cases} \quad (1).$$

Adopting the Clarke's transformation, the inductor currents and the capacitor voltage dynamic model for the three phase grid-tied inverter in αβ stationary reference frame are given as,

$$\frac{dx}{dt} = Ax + Bv_{i\alpha\beta} + B_d v_{g\alpha\beta} \quad (2),$$

where

$$x = \begin{bmatrix} i_{1\alpha\beta} \\ i_{2\alpha\beta} \\ u_{c\alpha\beta} \end{bmatrix}, A = \begin{bmatrix} 0 & 0 & -1/L_1 \\ 0 & 0 & 1/L_2 \\ 1/C & -1/C & 0 \end{bmatrix} \quad (3),$$

$$B = \begin{bmatrix} 1/L_1 & 0 & 0 \end{bmatrix}^T, B_d = \begin{bmatrix} 0 & -1/L_2 & 0 \end{bmatrix}^T \quad (4).$$

Next, according to the state-space model described in (2), the discrete time model of LCL filter based on the sampling time T_s can be obtained as,

$$x(k+1) = A_1 x(k) + B_1 v_i(k) + B_2 v_g(k) \quad (5),$$

where matrices A_1, B_1, and B_2 are

$$A_1 = e^{AT_s}, B_1 = \int_0^{T_s} e^{A\tau} B d\tau, B_2 = \int_0^{T_s} e^{A\tau} B_d d\tau \quad (6).$$

The detailed expressions of (6) can be found in the appendix.

B. Conventional FCS-MPC strategy

Unlike other common control algorithm applied in the grid-tied inverter, the FCS-MPC strategy does not adopt a modulation stage, but depends on a finite number of output voltage vectors of inverter, which can be obtained by utilizing a traversal method. These voltage vectors are used to minimize the selected cost function online, and then the optimal inverter output voltage vector can be captured.

The conventional FCS-MPC scheme is implemented in following steps [11],

1) Measure the inverter-side current, the grid-injected current, the capacitor voltage, and the grid voltage;
2) Calculate the reference of the capacitor voltage and the inverter-side current by utilizing the reference of grid-injected current;
3) Deduce the references of three state variables at next step using the Lagrangian Extrapolation;
4) Predict the values of three state variables in next sampling instant for all possible inverter output voltage vectors;
5) Construct the cost function;
6) Select the optimal inverter output voltage vector.

The conventional FCS-MPC strategy requires two kinds of current sensors for inductor current measurements and two types of voltage sensors for capacitor voltage and grid voltage measurements. Additionally, the computational delay was not taken into account, which may degrade the system performance and increase the ripples of grid-injected current. For the purpose of reducing the number of sensors and eliminating this

considerable computational delay, a novel control scheme with full status observations based on virtual flux and state observer is proposed in the following section, which only two grid-injected current sensors are used to generate the high quality grid-injected currents and achieve the grid synchronization.

III. PROPOSED FCS-MPC STRATEGY WITH FULL STATUS ESTIMATIONS BASED ON VIRTUAL FLUX AND STATE OBSERVER

The proposed FCS-MPC strategy with full status estimation based on virtual flux and state observer is depicted in Fig. 1. As shown in Fig. 1, only the grid-injected current sensors are utilized for measurement, and the other variables, including the inverter-side current, the capacitor voltage and the grid voltage, are estimated by the state observer and the virtual flux observer, respectively. However, it should be noticed that although the grid-injected currents are measured, the proposed FCS-MPC strategy does not utilize these measured variables for the control, but relies on all four observations.

The design process of proposed FCS-MPC method can be realized as follows:

Firstly, estimate the grid voltage and the reference value of grid-injected current by utilizing the virtual flux observer, based on the measured grid-injected currents, active power, reactive power and the switching state $S(k)$ at k^{th} instant, where this switching state is calculated in the last period.

Secondly, estimate the inverter-side inductor currents, the grid-injected currents, and the capacitor voltages by adopting the state observer, which is based on the observed grid voltages and the measured grid-injected currents.

Thirdly, predict the three observed state variables at the $(k+2)^{th}$ instant, based on the discrete time model of LCL filter described in (5).

Next, obtain the references of inverter-side inductor currents and capacitor voltages as,

$$\begin{cases} u_{c\alpha\beta}^* = \hat{v}_{g\alpha\beta} - \omega L_2(i_{2\beta}^* - ji_{2\alpha}^*) \\ i_{1\alpha\beta}^* = (1-\omega^2 L_2 C)i_{2\alpha\beta}^* \end{cases} \tag{7}.$$

Then, calculate the reference x at the $(k+2)^{th}$ instant utilizing the Lagrangian Extrapolation, and it can be expressed as,

$$x_{\alpha\beta}^*(k+2) = 6x_{\alpha\beta}^*(k) - 8x_{\alpha\beta}^*(k-1) + 3x_{\alpha\beta}^*(k-2) \tag{8},$$

where $x = [i_1 \ i_2 \ u_c]^T$.

According to the analysis mentioned above, the cost function is constructed, which includes the errors between three estimated state variables and their references in this paper. However, due to the different nature (including different units and magnitudes) for three state variables, a suitable weighting factor is necessary, which can regulate the influences of variables on the cost function. Therefore, the modified cost function based on full status estimations and delay compensation can be expressed as,

$$J = (\varepsilon_{i1\alpha}^2(k+2) + \varepsilon_{i1\beta}^2(k+2)) + \lambda_{i2}(\varepsilon_{i2\alpha}^2(k+2) + \varepsilon_{i2\beta}^2(k+2)) + \lambda_{uc}(\varepsilon_{uc\alpha}^2(k+2) + \varepsilon_{uc\beta}^2(k+2)) \tag{9},$$

where ε is the error of controlled variables between reference value and estimated value. The weighting factor λ_{uc} is set to achieve active damping [28], and λ_{i2} is tuned to obtain a high

quality grid-injected current [11]. And the weighting factors included in Table I are designed according to [29].

Finally, the optimal switching state, which is employed at $(k+1)^{th}$ instant, is selected based on the modified cost function.

A. Virtual Flux Observer

1) The Concept of Virtual Flux

Generally, the grid voltage of grid-tied inverter connecting with L filter and resistance R can be considered as a virtual AC electric motor [30]. Furthermore, R and L in the inverter represent the corresponding the stator resistance and stator inductance in an AC motor, respectively. For the LCL-filter-based system, owing to the high impedance of filtering capacitor in low frequency, the fundament current of this capacitor can be treated as zero. Therefore, the currents of the grid-side and inverter-side inductors can be regarded as equal to each other, and we can utilize the sum of their inductances as the equivalent inductance. Consequently, neglecting R, the grid virtual flux vector in αβ coordinate system for grid-tied inverter with LCL filter can be deduced as,

$$\begin{cases} \psi_\alpha = \int v_{g\alpha} dt = \int (v_{i\alpha} - (L_1 + L_2)\frac{di_{2\alpha}}{dt}) \, dt \\ \psi_\beta = \int v_{g\beta} dt = \int (v_{i\beta} - (L_1 + L_2)\frac{di_{2\beta}}{dt}) \, dt \end{cases} \tag{10},$$

where ψ_α, ψ_β, $v_{g\alpha}$, $v_{g\beta}$, $v_{i\alpha}$, $v_{i\beta}$, $i_{2\alpha}$ and $i_{2\beta}$ are the component values of the virtual grid voltage flux vectors, the grid voltages, the optimal inverter output voltage vectors and the grid-injected currents in αβ coordinate system, respectively.

2) Amplitude and Phase Compensations

To eliminate undesired DC offsets associated with the integration, the flux observer in AC electric motor generally employs the first order low-pass filter to substitute the pure integrator. Thus, the same strategy is utilized for obtaining the virtual grid voltage flux in this paper. However, utilizing LPF will result in the errors of phase and amplitude, which deteriorates the performance of system. Therefore, in order to enhance the performance of grid-connected inverter, the phase and amplitude compensations are required to achieve the same effect of pure integrator, when utilizing the low-pass filter.

Assuming that $\psi_{\alpha\beta}$ is the virtual grid voltage flux described as complex space vector in αβ stationary reference frame,

$$\psi_{\alpha\beta} = \int v_g dt = \psi_\alpha + j\psi_\beta = |\psi| \angle \theta \tag{11}.$$

Adopting the first order low-pass filter, virtual grid voltage flux can be obtained as,

$$\psi_{\alpha\beta}' = \frac{v_g}{s + \omega_c} = |\psi'| \angle \theta' \tag{12},$$

$$\frac{\psi_{\alpha\beta}'}{\psi_{\alpha\beta}} = \frac{|\psi'|}{|\psi|} \angle (\theta' - \theta) = \frac{\omega_f}{\sqrt{\omega_f^2 + \omega_c^2}} \angle \varphi \tag{13},$$

where $\varphi = \pi/2 - \arctan(\omega_f/\omega_c)$, ω_f is the fundamental angular frequency and ω_c is the cut-off frequency, which usually can be set to $0.1\omega_f \sim 0.5\omega_f$.

According to the analysis above, the magnitude and the phase of the compensation gain is respectively $\sqrt{\omega_f^2 + \omega_c^2}/\omega_f$ and $\arctan(\omega_f/\omega_c) - \pi/2$.

3) The PLL Based on Virtual Flux

In order to realize the grid synchronization, the grid voltage phase angle or frequency should be detected. Since the satisfied results can be obtained by adjusting the bandwidth of PLL when grid voltage fluctuates, PLL is universally utilized as a common method to receive the information of the phase angle and frequency in power electronics. However, the voltage sensor, which provides the grid voltage phase angle and frequency, is not used in this paper. So, an approach based on VF is presented to estimate the phase angle and frequency, which has a great suppression on interference signal.

By adopting Clarke's transformation (equal amplitude transformation), the virtual flux in αβ coordinate system can be expressed as,

$$\begin{bmatrix} \psi_\alpha \\ \psi_\beta \end{bmatrix} = \psi \begin{bmatrix} \cos\theta \\ \sin\theta \end{bmatrix} \quad (14),$$

where ψ is the amplitude of virtual flux. And then, by utilizing the estimated grid voltage flux phase angle $\hat{\theta}$ of PLL output for synchronous rotating coordinate transformation, the virtual grid voltage flux in dq reference frame can be described as,

$$\begin{bmatrix} \psi_{de} \\ \psi_{qe} \end{bmatrix} = \begin{bmatrix} \cos\hat{\theta} & \sin\hat{\theta} \\ -\sin\hat{\theta} & \cos\hat{\theta} \end{bmatrix} \begin{bmatrix} \psi_\alpha \\ \psi_\beta \end{bmatrix} \quad (15).$$

Substituting (14) into (15), the flux components in dq axis can be represented in another form,

$$\begin{bmatrix} \psi_{de} \\ \psi_{qe} \end{bmatrix} = \psi \begin{bmatrix} \cos(\hat{\theta}-\theta) \\ -\sin(\hat{\theta}-\theta) \end{bmatrix} = \psi \begin{bmatrix} \cos(\Delta\theta) \\ -\sin(\Delta\theta) \end{bmatrix} \quad (16).$$

It can be seen from the (16), if the error $\Delta\theta$ between the estimated grid flux phase angle and the actual grid flux phase angle is equal to zero, i.e. $\psi_{de}=\psi$ and $\psi_{qe}=0$. Therefore, we can know that the actual grid flux can be locked immediately by adjusting $-\psi_{qe}$ to zero, which has the advantage that no information is required about the magnitude of the actual grid flux. The virtual grid voltage flux observer based on PLL is shown in Fig. 2.
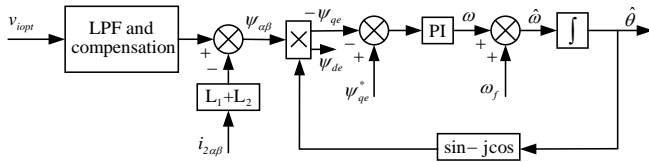

Fig. 2 Virtual grid voltage flux observer based on PLL

4) VF-based Grid Voltage Sequence Extraction Strategy

Under the balanced grid voltage condition, the grid voltage can be simply estimated by the expression of $\hat{v}_{g\alpha\beta} = j\omega_f \psi_{\alpha\beta}$ and $\hat{\theta}_g = \hat{\theta} + \pi/2$. However, for the unbalanced grid voltage, the relationship between the grid voltage and the virtual flux cannot be simply expressed as the expression mentioned above, due to the existence of negative sequence components of the unbalanced grid voltage. Thus, a VF-based grid voltage sequence extraction strategy is proposed to eliminate the adverse effects caused by the negative sequence components.

Under the unbalanced grid voltage condition, by neglecting the zero sequence components, the grid voltage can be described as the sum of positive- and negative-sequence components in αβ reference frame as

$$\begin{cases} v_{g\alpha} = v_{g\alpha}^p + v_{g\alpha}^n = V_g^p \cos(\hat{\omega}t + \varphi_p) + V_g^n \cos(-\hat{\omega}t + \varphi_n) \\ v_{g\beta} = v_{g\beta}^p + v_{g\beta}^n = V_g^p \sin(\hat{\omega}t + \varphi_p) + V_g^n \sin(-\hat{\omega}t + \varphi_n) \end{cases} \quad (17),$$

where $v_{g\alpha}^p$, $v_{g\beta}^p$ and $v_{g\alpha}^n$, $v_{g\beta}^n$ are the positive- and negative-sequence components of the grid voltage in αβ reference frame, V_g is the amplitude of the grid voltage, and φ_p and φ_n are the initial phase angle, $\hat{\omega}$ is the grid angular frequency.

Considering the negative-sequence components of the grid voltage are not zero under unbalanced grid voltage, the virtual grid voltage flux can be expressed as follows:

$$\begin{cases} \psi_\alpha = \int v_{g\alpha}dt = \dfrac{1}{\omega}(v_g^p \sin(\hat{\omega}t + \varphi_p) - v_g^n \sin(-\hat{\omega}t + \varphi_n)) = \dfrac{1}{\omega}(v_{g\beta}^p - v_{g\beta}^n) \\ \psi_\beta = \int v_{g\beta}dt = \dfrac{1}{\omega}(-v_g^p \cos(\hat{\omega}t + \varphi_p) + v_g^n \cos(-\hat{\omega}t + \varphi_n)) = \dfrac{1}{\omega}(-v_{g\alpha}^p + v_{g\alpha}^n) \end{cases}$$
$$(18).$$

Combining (17) with (18), the positive- and negative-sequence components of the grid voltage can be obtained as

$$\begin{cases} v_{g\alpha}^p = (v_{g\alpha} - \hat{\omega}\psi_\beta)/2 \\ v_{g\alpha}^n = (v_{g\alpha} + \hat{\omega}\psi_\beta)/2 \\ v_{g\beta}^p = (v_{g\beta} + \hat{\omega}\psi_\alpha)/2 \\ v_{g\beta}^n = (v_{g\beta} - \hat{\omega}\psi_\alpha)/2 \end{cases} \quad (19),$$

where the grid voltage in αβ reference frame is estimated by utilizing the second order generalized integrator-based quadrature signal generator (SOGI-QSG) [31], $\hat{\omega}$ is the grid angular frequency obtained by the PLL. And the analysis process is shown in the following part.

By neglecting the current of filtering capacitor, the continue-time model of grid-tied inverter with LCL filter in αβ coordinate system can be represented as

$$\begin{bmatrix} v_{g\alpha} \\ v_{g\beta} \end{bmatrix} = \begin{bmatrix} v_{i\alpha} \\ v_{i\beta} \end{bmatrix} - (L_1 + L_2)\frac{d}{dt}\begin{bmatrix} i_{2\alpha} \\ i_{2\beta} \end{bmatrix} \quad (20).$$

Since the in-phase and in-quadrature signals of the input signal can be obtained by using SOGI-QSG [31], and the differential of the sinusoidal signal can be transformed into the in-phase or inverted value of its quadrature signal. Equation (20) can be written in the following form,

$$\begin{bmatrix} \hat{v}_{g\alpha} \\ \hat{v}_{g\beta} \end{bmatrix} = \begin{bmatrix} \hat{v}_{i\alpha} \\ \hat{v}_{i\beta} \end{bmatrix} + \hat{\omega}(L_1 + L_2)\begin{bmatrix} \hat{i}_{2\alpha}^\perp \\ \hat{i}_{2\beta}^\perp \end{bmatrix} \quad (21),$$

where $\hat{v}_{g\alpha}$ and $\hat{v}_{g\beta}$ are the estimated grid voltage in αβ coordinate system. $\hat{v}_{i\alpha}$, $\hat{v}_{i\beta}$ and $\hat{i}_{2\alpha}^\perp$, $\hat{i}_{2\beta}^\perp$ are the in-phase and in-quadrature signals of the input inverter-side voltage and grid-injected current respectively.

Substituting (21) into (19), the positive- and negative-sequence components of the grid voltage in αβ coordinate system can be deduced. Then, in order to get the balanced and sinusoidal grid-injected current, the negative sequence components of the grid-injected current are regarded as zero and the positive sequence components of the grid-injected current should satisfy the equations of $\bar{P} = P_{ref}$ and $\bar{Q} = Q_{ref}$ [32]. Hence, the reference of the grid-injected current in αβ

coordinate system can be deduced ($P_{ref} = 3$ kW, $Q_{ref} = 0$ var in this paper) as

$$\begin{bmatrix} i_{2\alpha}^* \\ i_{2\beta}^* \end{bmatrix} = \frac{2P_{ref}}{3[(\hat{v}_{g\alpha}^p)^2 + (\hat{v}_{g\beta}^p)^2]} \begin{bmatrix} \hat{v}_{g\alpha}^p \\ \hat{v}_{g\beta}^p \end{bmatrix} + \frac{2Q_{ref}}{3[(\hat{v}_{g\alpha}^p)^2 + (\hat{v}_{g\beta}^p)^2]} \begin{bmatrix} \hat{v}_{g\beta}^p \\ -\hat{v}_{g\alpha}^p \end{bmatrix} \quad (22).$$

B. State Observer

The predictions in next sampling instant need to be calculated by utilizing the predictive discrete time model expressed in (5) for the FCS-MPC algorithm. However, it is worth noting that for evaluating (5), besides the grid voltage estimated by virtual flux observer, it is necessary to measure the inverter-side inductor currents, the capacitor voltages and the grid-injected currents. These state variables can be probed by current and voltage sensors, but increasing the cost and complexity of system. Therefore, to avoid the additional sensors, a full-order observer is adopted to estimate the inverter-side inductor currents, the capacitor voltages and the grid-injected currents based on the measured grid-injected current in this paper.
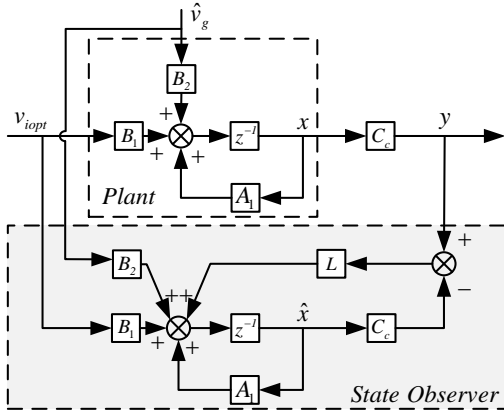

Fig. 3 Structure frame of the state observer

As seen in Fig. 3, the state observer, which is based on the discrete time model of the LCL filter in (5), has the merits that the state variables can be observed according to one of the measured state variables. Considering the error between the estimated and the actual state variables caused by model mismatch and parameter drift, the observer feedback gain vector L based on the measured and observed variables is introduced, which can make the performance of state observer satisfy the certain design standards.

The state-space model of the state observer in the discrete time-domain can be expressed as,

$$\begin{cases} \hat{x}(k+1) = A_1\hat{x}(k) + B_1 v_{iopt}(k) + B_2\hat{v}_g(k) + L(y(k) - \hat{y}(k)) \\ \hat{y}(k) = C_c\hat{x}(k) \end{cases} \quad (23),$$

where $L = [l_1 \ l_2 \ l_3]^T$ denotes the observer feedback gain vector and $C_c = [0 \ 1 \ 0]$ is the output matrix, which represents the measured state variable (grid-injected current in this paper). As expressed in (24), it can be found that the observability matrix is full rank, which indicates that the system is observable. Consequently, the eigenvalues of state observer can be assigned arbitrarily.

$$rank \begin{bmatrix} C_c \\ C_c A_1 \\ C_c A_1^2 \end{bmatrix} = 3 \quad (24).$$

The dynamics of state observation error is derived as,

$$\Delta x(k+1) = x(k+1) - \hat{x}(k+1) = (A_1 - LC_c)\Delta x(k) \quad (25).$$

The conclusion we can draw from (25) that if the matrix of A_1-LC_c is Hurwitz, the observation error is asymptotically stable. According to pole placement of the state observer, the characteristic polynomial of the observer can be set as,

$$\det(zI - A_1 + LC_c) = (z - p_1)(z - p_2)(z - p_3) \quad (26),$$

where p_1, p_2 and p_3 are the desired poles of the state observer. In order to acquire the values of L, these desired poles of the state observer need to be ensured. It is typically easier to identify the poles first in the s-domain and then map them to the z-domain via $z = \exp(sT_s)$. In the s-domain, the closed-loop characteristic polynomial can be expressed as $(s + \alpha_{od})(s^2 + 2\zeta_{or}\omega_{or}s + \omega_{or}^2)$. Then, the poles p_1, p_2 and p_3 in the z-domain can be described in (27). Thus, the observer gain vector L can be deduced by solving the equation (26). A simple method to solve the equation (26) is using the MATLAB function, i.e. $acker$. And, $L = [-0.4196 \ 1.1663 \ 11.9272]^T$ is adopted in this paper.

$$\begin{cases} p_1 = \exp(-\alpha_{od}T_s) \\ p_{2,3} = \exp[(-\zeta_{or} \pm j\sqrt{1 - \zeta_{or}^2})\omega_{or}T_s] \end{cases} \quad (27)$$

The pair of complex-conjugate poles, determined by ζ_{or} and ω_{or}, are set to decide the dominant dynamics of the estimation errors. The real pole α_{od} is located at a higher frequency. ζ_{or} is the damping ratio, usually set as 0.707. The range of the natural frequency ω_{or} with respect to the resonance frequency of LCL filter is regarded from 0.5 to 1. And the value of α_{od} is 5~10 times larger than the pair of complex-conjugate poles. A rule of thumb to choose the observer poles is to make them several times faster than the open-loop system dynamics.

C. Computational Delay Compensation

For the conventional FCS-MPC algorithm mentioned in Section II, the computational time is not addressed. However, when applying a dSPACE platform or DSP to verify the control strategy in practical systems, the calculations are time consuming and it will lead to a computational delay, which may degrade the control effect. Therefore, even if this computational time is very short, it also needs to be taken into account in the control algorithm. Otherwise, the system performance will be greatly degraded.
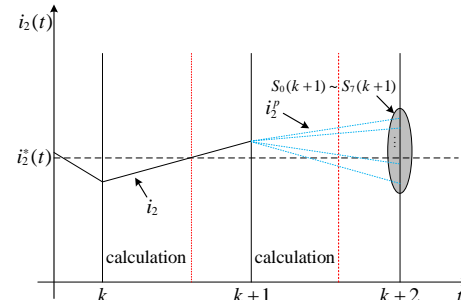

Fig. 4. Operation of the proposed FCS-MPC method for LCL-filter-based grid-tied inverter with delay compensation.

As displayed in Fig. 4, assuming that the computational time is not negligible compared with the sampling time, there will be a delay between the sampling and the action instant of new switching state. In order to eliminate the influence of the computational delay, the control algorithm with delay compensation is presented, and its operation process is described in Fig. 4. Firstly, the estimated variables obtained from the state observer and the inverter output voltage vector at t_k obtained at t_{k-1} are applied in (5) to predict three state variables in next sampling interval. Then, the discrete-time LCL filter model is shifted one step forward in time and those three state variables at t_{k+1} are employed as starting points for the next-step predictions. Next, the predictions at t_{k+2} can be obtained by using seven different inverter output voltage vector. Finally, these predictions are taken into the cost function for evaluating. The switching state, which minimizes the cost function, is selected and stored to be applied at next sampling instant.

D. Overcurrent protection

Generally, there is an overshoot current at the first period for the sensorless control method, since the observations do not have any information until the system starts up. It also exists in the proposed control method in this paper. The approach of solving the overcurrent phenomena as described below can be also found in IV-C of [33].

Based on the proposed cost function J in this paper, an additional term $h_{\lim}$, which is used to realize overcurrent protection, is added. It is defined in the following type:

$$h_{\lim} = \begin{cases} \infty & i_2 \geq I_{\max} \\ 0 & i_2 < I_{\max} \end{cases} \tag{28}$$

where $I_{\max}$ is the current protection value.

Thus, the cost function can be further expressed as:

$$J_1 = J + h_{\lim} \tag{29}$$

It can be seen from (28), if the amplitude of the grid-injected current is larger than the current protection value $I_{\max}$, the additional term $h_{\lim}$ of the cost function J_1 will be set to ∞. Therefore, the cost function J_1 will be considered to ∞, and the corresponding inverter voltage vector v_i will not be chosen. If the amplitude of the grid-injected current is smaller than the current protection value $I_{\max}$, the additional term $h_{\lim}$ of the cost function J_1 will be set to zero, and it will not affect the original cost function J. Consequently, this method can successfully realize overcurrent protection.

IV. EXPERIMENTAL RESULTS

Since a large amount of sensors are used for the conventional FCS-MPC algorithms applied in the grid-tied inverter with LCL filter, a novel FCS-MPC strategy based on full status estimations is proposed to reduce the number of sensors, but not deteriorate the performance of system. The performance of the proposed FCS-MPC strategy with full status estimations based on virtual flux and state observer are evaluated under both balanced and unbalanced grid voltage condition on a laboratory test-rig. The programmable ac source (Chroma 61830) is used

to simulate the grid. The power stage consists of a two-level voltage-source inverter (Danfoss-FC320) with a dc-link voltage provided by Chroma 62150H-600S DC power supply. The digital control algorithm is implemented in dSPACE 1202 platform, where a controldesk project is developed to tune control parameter and reference value, as well as display the observation results which cannot be captured by Yokogawa DL 1640 digital oscilloscope. It should be noticed that the following waveforms are all based on pure observations throughout the experiment. In all measured signals, including the grid voltage, the grid-injected current, the capacitor voltage and the inverter-side inductor current, only the grid-injected current is applied for VF observer and state observer estimation. The other measured signals are only utilized for comparisons with the observation results. The experimental parameters are listed in Table I.

TABLE I
SYSTEM VARIABLES AND PARAMETERS

Variable	Parameters	Value
v_g	Grid voltage	110V$_{\text{RMS}}$
U_{dc}	DC voltage	350V
L_1	Inverter-side inductance	3.6mH
L_2	Grid-side inductance	2.8mH
C	LCL filter capacitance	12μF
T_s	Sampling time	40μs
f_{sw}	Average switching frequency	5.8 kHz
λ_{uc}	Weighting factor of capacitor voltage	0.0826
λ_{i2}	Weighting factor of grid-injected current	87
L	Gain vector	$[-0.4196\ 1.1663\ 11.9272]^T$

A. Estimated Results of State Variables and Grid Voltage

Fig. 5 shows the steady-state estimation waveforms of state variables and grid voltage captured by the controldesk project. It can be found that the estimations are consistent with the measurements, and the errors of them caused by uncertain disturbance are relatively small, which can be acceptable.

The performance of the state observer and virtual flux observer also should be evaluated during a transient response for assessing the performance of the overall system. Fig. 6 displays the transient observation waveforms of the state variables and the grid voltage. The reference of active power is set at a value of 1.5 kW and then stepped up to 3 kW, i.e. the reference of grid-injected current is set at a value of 6.28 A (peak) and then stepped up to 12.86 A (peak). The experimental results demonstrate that, the state observer and the virtual flux observer estimate the state variables and the grid voltage accurately, and the observation of grid-injected current reaches to its steady state in approximately 2 ms, performing a good dynamic response.

B. Experimental Results under Balanced Grid Voltage

1) Starting process

Unlike the conventional measurement-based control, the sensorless control cannot give as good operation in the first period, because the estimations do not have any information until the system starts up. Fig. 7 displays the transient waveforms of grid-injected current after starting up. By the pro-
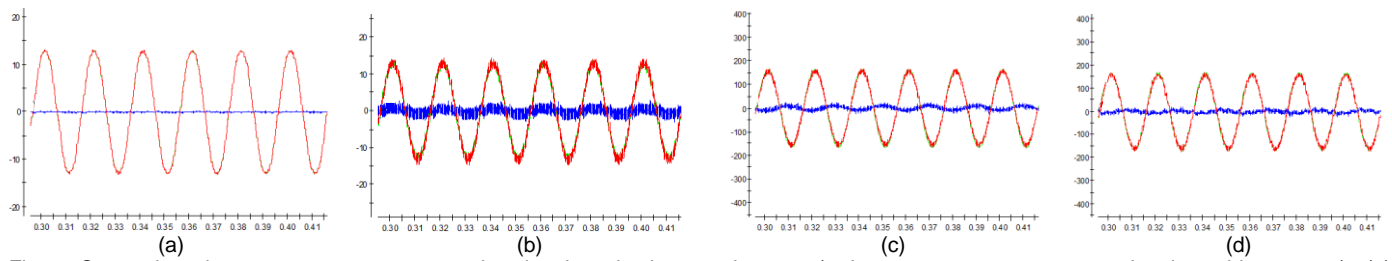
Fig. 5 Comparison between measurements and estimations in the steady state (red: measurements, green: estimations, blue: errors): (a) grid-injected current, (b) inverter-side current, (c) grid voltage, (d) capacitor voltage.
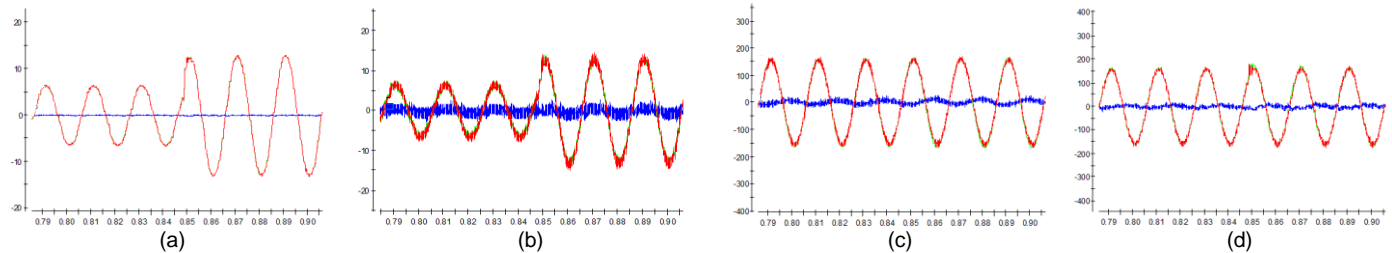

Fig. 6 Comparison between measurements and estimations at transient state condition (red: measurements, green: estimations, blue: errors): (a) grid-injected current, (b) inverter-side current, (c) grid voltage, (d) capacitor voltage.
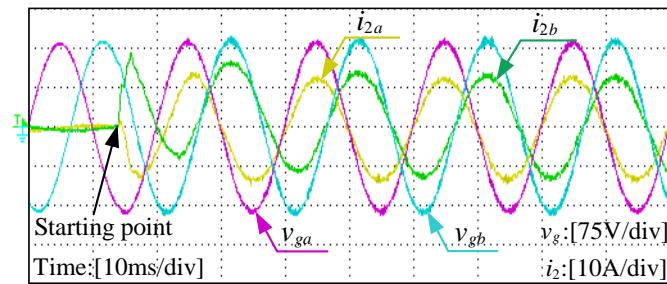

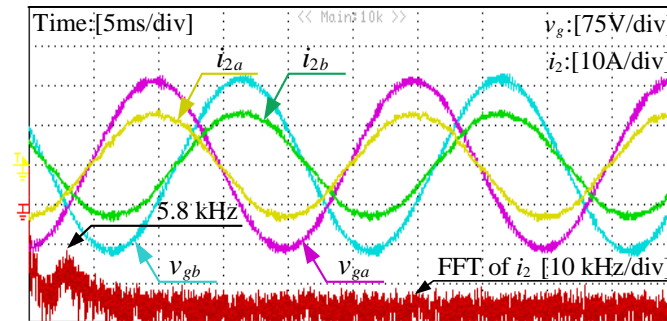Fig. 7 The starting process of the proposed control method with overcurrent protection.

Fig. 8 Experimental steady-state waveforms and the harmonic spectrum of grid-side current under the stiff grid condition.

posed control strategy with overcurrent protection, the system can converge and achieve grid synchronization after one and a half grid period. It can be illustrated that the strategy of overcurrent protection is effective.

2) Steady State Waveforms

The experimental steady-state waveforms and the harmonic spectrum of grid-injected current under the stiff grid condition are depicted in Fig. 8. Due to the limitation of the experimental device, only a-phase and b-phase currents are measured. It can be seen that the grid-injected current is sinusoidal with low THD and the average switching frequency is about 5.8 kHz. And, the grid synchronization is achieved, which enhances the

energy efficiency via unity power factor operation.

3) Dynamic State Performance

Fig. 9 displays the experimental transient waveforms of grid-injected current and grid voltage under the stiff grid condition when the reference of active power steps up from 1.5 kW to 3 kW, and steps down from 3 kW to 1.5 kW, respectively. (i.e. the reference of grid-injected current amplitude steps up from 6.43 A to 12.86 A, and steps down from 12.86 A to 6.43 A, respectively). The experimental results demonstrate that the grid-injected current is able to accurately track the reference within approximately 2 ms, reflecting the good dynamic response and reliability of proposed control method. Fig. 10 illustrates the experimental result of the grid-injected current with sharp phase angle variation from 0° to 30°. It can be seen from Fig. 10 that the effectiveness and good dynamic response for adjusting the power factor can be achieved by using the proposed control strategy. Fig. 11 shows the experimental waveforms of grid-injected current and grid voltage for a 25% three phase grid voltages dip, and it can be concluded that grid-injected current can track the reference value accurately and quickly so that keep the active power constant.

4) Parameter Mismatch Influence

Model parameter mismatch error is unavoidable for observations due to the must-use of system model. The weak grid is one of the most common parameter mismatch situations. Due to the possible wide variation of grid impedance in the actual grid, this weak grid situation should be emulated by adding the additional grid inductance L_g in the experimental tests. As depicted in Fig. 12, it shows the experimental transient waveforms of grid-injected current and grid voltage under weak grid condition (L_g=4 mH) when the reference of active power steps down from 3 kW to 1.5 kW. It can be seen from Fig. 12 that the proposed control strategy is robust against the grid impedance variations, and it also has a good dynamic response even under the weak grid condition. To further verify the robustness of proposed control strategy, the inverter-side indu-
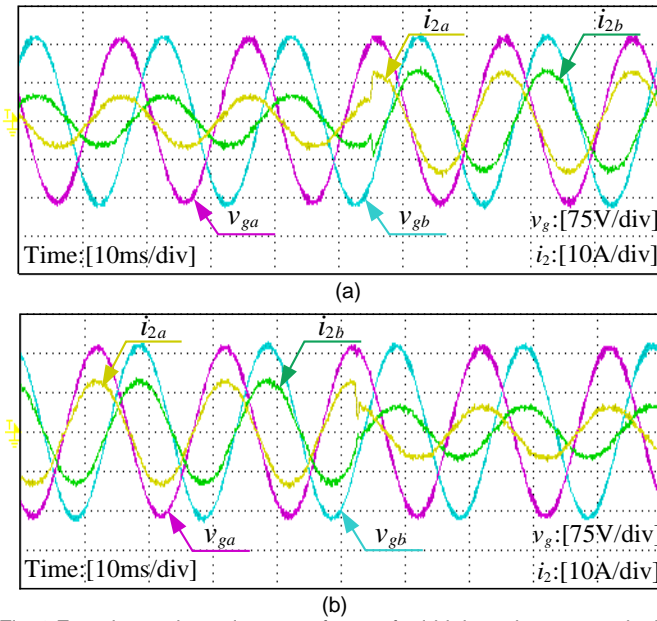
(a)

(b)

Fig. 9 Experimental transient waveforms of grid-injected current and grid voltage under the stiff grid condition: (a) step-up from 1.5 kW to 3 kW, (b) step-down from 3 kW to 1.5 kW.
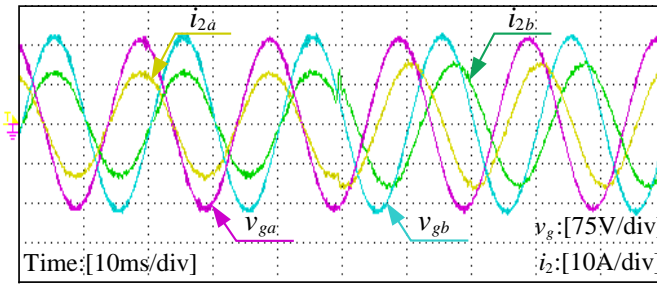

Fig. 10. Experimental waveforms of grid-injected current with sharp phase angle variation from 0° to 30°.
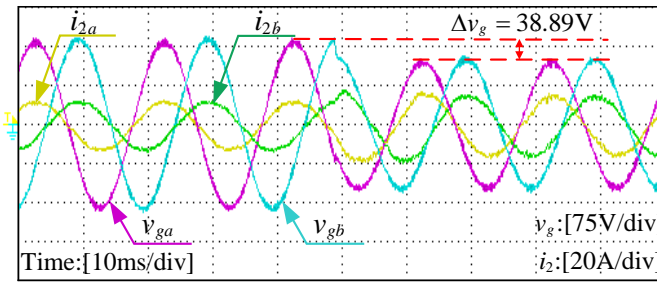

Fig. 11 Experimental waveforms of grid-injected current and grid voltage for a 25% three phase grid voltages dip.
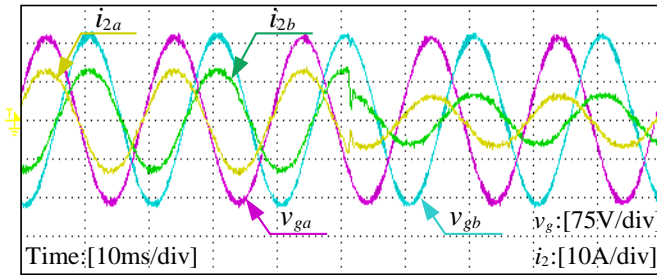

Fig. 12 Experimental transient waveforms of grid-injected current and grid voltage under the weak grid condition (L_g=4 mH).
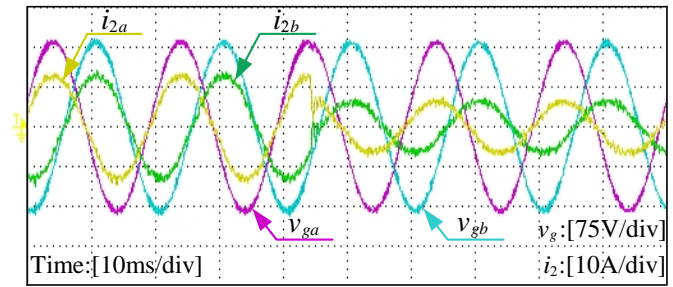

Fig. 13. Experimental waveforms of grid-injected current with filter parameter mismatch (L_1= 2.4 mH, C =9 µF, L_2 = 2 mH).
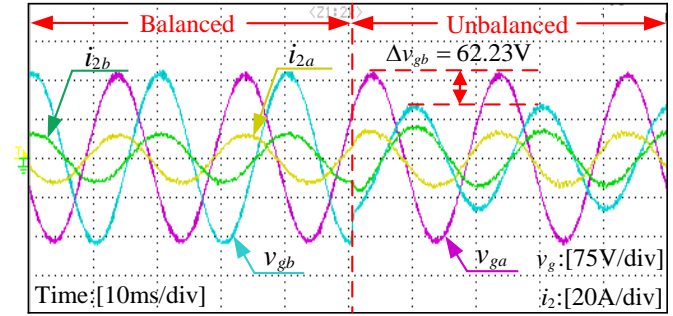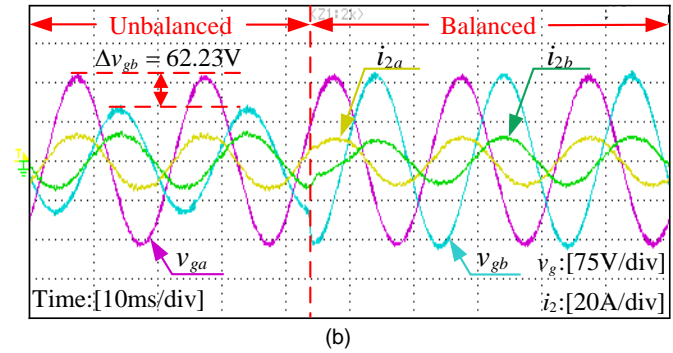

(a)

(b)

Fig. 14 Experimental waveforms of grid-injected current when grid voltage varies (a) from balance to unbalance; (b) from unbalance to balance.

ctor L_1 decreases from 3.6 mH to 2.4 mH (33.3% dips), the grid-side inductor L_2 reduces from 2.8 mH to 2 mH (28.6% dips), the filtering capacitor C drops from 12 µF to 9 µF (25% dips), simultaneously. The experimental result of grid-injected current is shown in Fig. 13. It can be illustrated that the robustness against parameter mismatch is great.

C. Experimental Results under Unbalanced Grid Voltage

1) Under Undistorted Grid Voltage

The voltage dip is generally caused by the failure of the power grid like short circuit faults, or sudden changes in the load, such as the start of high-power equipment. It can cause many problems in control of the inverter. Fig. 14 demonstrates experimental results of grid-injected current when grid voltage varies from balance to unbalance and changes from unbalance to balance. The unbalanced grid voltage is emulated by 40% grid voltage dip in phase B. As depicted in Fig. 14, the grid-injected currents are balanced under both balanced and unbalanced grid voltage conditions, and the dynamic response is fast. It can sufficiently verify the effectiveness of proposed FCS-MPC strategy under unbalanced grid voltage condition.

2) Under Distorted Grid Voltage

Actually, in the case of grid voltage dips, often accompanied by harmonics. Thus, the proposed control algorithm should also be robust enough to handle this kind of disturbance. Fig.15 shows the experimental waveforms of grid-injected current and grid voltage under both unbalanced and distorted grid voltage. The unbalanced grid voltage is emulated by 40% grid voltage dip in phase B. The grid voltage is distorted by the 3rd, 5th, 7th and 9th harmonics, whose magnitudes with respect to the grid fundamental voltage are 3%, 3%, 3%, 3%, respectively. The experimental result displays an almost sinusoidal current waveform, which is mainly due to the low equivalent switching frequency of 5.8 kHz.
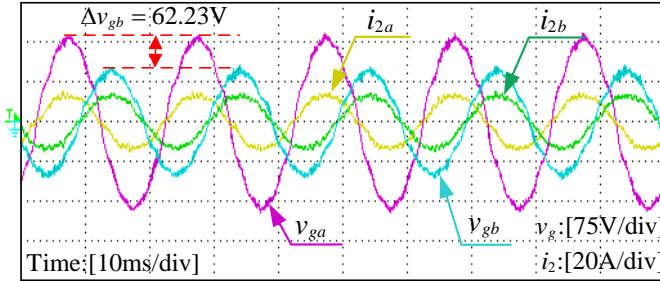

Fig. 15 Experimental waveforms of grid-injected current and grid voltage under both unbalanced and distorted grid voltages.

V. CONCLUSION

In this paper, a novel FCS-MPC strategy with full status observations based on virtual flux and state observer is proposed for the LCL-filtered grid-tied inverter. A step-by-step design procedure of the proposed control strategy is described in detail. A 3-kW/3-phase/110V experimental platform is established to verify the performance of proposed control scheme. By theoretical analysis and experimental verification, following conclusions can be drawn:

1) The proposed control strategy can achieve the grid synchronization, the delay compensation, and the high quality grid-injected current both under balanced and unbalanced grid voltage condition. Note that only the grid-injected current is measured.

2) The proposed strategy can be applied as the backup control of system by utilizing other control method with more sensors, where the grid-tied inverter still need operate under some sensor-fault conditions. Therefore, as a backup control, the proposed strategy shall inevitably improve the control reliability and enhance the sensor fault-through capacity of original system. Certainly, it may be at the cost of performance degradation, due to the switching and sampling frequencies.

APPENDIX

$$A_1 = \begin{bmatrix} \dfrac{L_1 + L_2\cos(\omega_{res}T_s)}{L_1 + L_2} & \dfrac{L_2(1-\cos(\omega_{res}T_s))}{L_1 + L_2} & -\dfrac{\sin(\omega_{res}T_s)}{\omega_{res}L_1} \\[2ex] \dfrac{L_1(1-\cos(\omega_{res}T_s))}{L_1 + L_2} & \dfrac{L_2 + L_1\cos(\omega_{res}T_s)}{L_1 + L_2} & \dfrac{\sin(\omega_{res}T_s)}{\omega_{res}L_2} \\[2ex] \dfrac{\sin(\omega_{res}T_s)}{\omega_{res}C} & -\dfrac{\sin(\omega_{res}T_s)}{\omega_{res}C} & \cos(\omega_{res}T_s) \end{bmatrix},$$

$$B_1 = \begin{bmatrix} \dfrac{T_s}{L_1 + L_2} + \dfrac{L_2\sin(\omega_{res}T_s)}{L_1(L_1 + L_2)\omega_{res}} \\[2ex] \dfrac{T_s}{L_1 + L_2} - \dfrac{\sin(\omega_{res}T_s)}{(L_1 + L_2)\omega_{res}} \\[2ex] \dfrac{L_2(1-\cos(\omega_{res}T_s))}{L_1 + L_2} \end{bmatrix},$$

$$B_2 = \begin{bmatrix} -\dfrac{T_s}{L_1 + L_2} + \dfrac{\sin(\omega_{res}T_s)}{(L_1 + L_2)\omega_{res}} \\[2ex] -\dfrac{T_s}{L_1 + L_2} - \dfrac{L_1\sin(\omega_{res}T_s)}{L_2(L_1 + L_2)\omega_{res}} \\[2ex] \dfrac{L_1(1-\cos(\omega_{res}T_s))}{L_1 + L_2} \end{bmatrix}, \text{ where } \omega_{res} = \sqrt{\dfrac{L_1 + L_2}{L_1 L_2 C}}.$$

REFERENCES

[1] F. Blaabjerg, Y. Yang, D. Yang and X. Wang, "Distributed Power-Generation Systems and Protection," *Proc. of the IEEE*, vol. 105, no. 7, pp. 1311-1331, July 2017.

[2] X. Li, H. Zhang, M. B. Shadmand and R. S. Balog, "Model Predictive Control of a Voltage-Source Inverter With Seamless Transition Between Islanded and Grid-Connected Operations," *IEEE Trans. Ind. Electron.*, vol. 64, no. 10, pp. 7906-7918, Oct. 2017.

[3] S. Kouro, J. I. Leon, D. Vinnikov and L. G. Franquelo, "Grid-Connected Photovoltaic Systems: An Overview of Recent Research and Emerging PV Converter Technology," *IEEE Ind. Electron. Mag.*, vol. 9, no. 1, pp. 47-61, March 2015.

[4] W. Wu, Y. Liu, Y. He, H. S. Chung, M. Liserre and F. Blaabjerg, "Damping Methods for Resonances Caused by LCL-Filter-Based Current-Controlled Grid-Tied Power Inverters: An Overview," *IEEE Trans. Ind. Electron.*, vol. 64, no. 9, pp. 7402-7413, Sept. 2017.

[5] Y. Liu, W. Wu, Y. He, Z. Lin, F. Blaabjerg and H. S. Chung, "An Efficient and Robust Hybrid Damper for LCL-or LLCL-Based Grid-Tied Inverter With Strong Grid-Side Harmonic Voltage Effect Rejection," *IEEE Trans. Ind. Electron.*, vol. 63, no. 2, pp. 926-936, Feb. 2016.

[6] R. P. Vieira, L. T. Martins, J. R. Massing and M. Stefanello, "Sliding Mode Controller in a Multiloop Framework for a Grid-Connected VSI With LCL Filter," *IEEE Trans. Ind. Electron.*, vol. 65, no. 6, pp. 4714-4723, June 2018.

[7] X. Mu, J. Wang, W. Wu and F. Blaabjerg, "A Modified Multifrequency Passivity-Based Control for Shunt Active Power Filter With Model-Parameter-Adaptive Capability," *IEEE Trans. Ind. Electron.*, vol. 65, no. 1, pp. 760-769, Jan. 2018.

[8] P. Cortes, M. P. Kazmierkowski, R. M. Kennel, D. E. Quevedo and J. Rodriguez, "Predictive Control in Power Electronics and Drives," *IEEE Trans. Ind. Electron.*, vol. 55, no. 12, pp. 4312-4324, Dec. 2008.

[9] S. Vazquez et al., "Model Predictive Control: A Review of Its Applications in Power Electronics," *IEEE Ind. Electron. Mag.*, vol. 8, no. 1, pp. 16-31, March 2014.

[10] S. Vazquez, J. Rodriguez, M. Rivera, L. G. Franquelo and M. Norambuena, "Model Predictive Control for Power Converters and Drives: Advances and Trends," *IEEE Trans. Ind. Electron.*, vol. 64, no. 2, pp. 935-947, Feb. 2017.

[11] P. Falkowski and A. Sikorski, "Finite Control Set Model Predictive Control for Grid-Connected AC–DC Converters With LCL Filter," *IEEE Trans. Ind. Electron.*, vol. 65, no. 4, pp. 2844-2852, April 2018.

[12] M. Parvez Akter, S. Mekhilef, N. Mei Lin Tan and H. Akagi, "Modified Model Predictive Control of a Bidirectional AC‒DC Converter Based on Lyapunov Function for Energy Storage Systems," *IEEE Trans. Ind. Electron.*, vol. 63, no. 2, pp. 704-715, Feb. 2016.

[13] Z. Ma, S. Saeidi and R. Kennel, "FPGA Implementation of Model Predictive Control With Constant Switching Frequency for PMSM Drives," *IEEE Trans. Ind. Informat.*, vol. 10, no. 4, pp. 2055-2063, Nov. 2014.

[14] S. Kouro, P. Cortes, R. Vargas, U. Ammann and J. Rodriguez, "Model Predictive Control—A Simple and Powerful Method to Control Power Converters," *IEEE Trans. Ind. Electron.*, vol. 56, no. 6, pp. 1826-1838, June 2009.

[15] J. Rodriguez et al., "State of the Art of Finite Control Set Model Predictive Control in Power Electronics," *IEEE Trans. Ind. Informat.*, vol. 9, no. 2, pp. 1003-1016, May 2013.

[16] V. Yaramasu, M. Rivera, B. Wu and J. Rodriguez, "Model Predictive Current Control of Two-Level Four-Leg Inverters—Part I: Concept, Algorithm, and Simulation Analysis," *IEEE Trans. Power Electron.*, vol. 28, no. 7, pp. 3459-3468, July 2013.

[17] C. Xia, T. Liu, T. Shi and Z. Song, "A Simplified Finite-Control-Set Model-Predictive Control for Power Converters," *IEEE Trans. Ind. Informat.*, vol. 10, no. 2, pp. 991-1002, May 2014.

[18] X. Wang, F. Blaabjerg and P. C. Loh, "Grid-Current-Feedback Active Damping for LCL Resonance in Grid-Connected Voltage-Source Converters," *IEEE Trans. Power Electron.*, vol. 31, no. 1, pp. 213-223, Jan. 2016.

[19] V. Miskovic, V. Blasko, T. M. Jahns, A. H. C. Smith and C. Romenesko, "Observer-Based Active Damping of LCL Resonance in Grid-Connected Voltage Source Converters," *IEEE Trans. Ind. Appl.*, vol. 50, no. 6, pp. 3977-3985, Nov.-Dec. 2014.

[20] J. Kukkola and M. Hinkkanen, "State Observer for Grid-Voltage Sensorless Control of a Converter Under Unbalanced Conditions," *IEEE Trans. Ind. Appl.*, vol. 54, no. 1, pp. 286-297, Jan.-Feb. 2018.

[21] F. Huerta, D. Pizarro, S. Cobreces, F. J. Rodriguez, C. Giron and A. Rodriguez, "LQG Servo Controller for the Current Control of LCL Grid-Connected Voltage-Source Converters," *IEEE Trans. Ind. Electron.*, vol. 59, no. 11, pp. 4272-4284, Nov. 2012.

[22] J. M. Kanieski, R. Cardoso, H. Pinheiro and H. A. Gründling, "Kalman Filter-Based Control System for Power Quality Conditioning Devices," *IEEE Trans. Ind. Electron.*, vol. 60, no. 11, pp. 5214-5227, Nov. 2013.

[23] R. Guzman, L. G. de Vicuña, J. Morales, M. Castilla and J. Miret, "Model-Based Control for a Three-Phase Shunt Active Power Filter," *IEEE Trans. Ind. Electron.*, vol. 63, no. 7, pp. 3998-4007, July 2016.

[24] H. Gholami-Khesht, M. Monfared and S. Golestan, "Low computational burden grid voltage estimation for grid connected voltage source converter-based power applications," *IET Power Electron.*, vol. 8, no. 5, pp. 656-664, 5 2015.

[25] A. A. Ghodke and K. Chatterjee, "One-cycle-controlled bidirectional three-phase unity power factor ac-dc converter without having voltage sensors," *IET Power Electron.*, vol. 5, no. 9, pp. 1944-1955, November 2012.

[26] J. Kim and S. Kwak, "Model Predictive Virtual Flux Control to Improve Performance Under Distorted Input Voltage Conditions," *IEEE Access*, vol. 6, pp. 34921-34933, 2018.

[27] H. Zhang, X. Zhu, J. Shi, L. Tan, C. Zhang and K. Hu, "Study on PWM Rectifier Without Grid Voltage Sensor Based on Virtual Flux Delay Compensation Algorithm," *IEEE Trans. Power Electron.*, vol. 34, no. 1, pp. 849-862, Jan. 2019.

[28] N. Panten, N. Hoffmann and F. W. Fuchs, "Finite Control Set Model Predictive Current Control for Grid-Connected Voltage-Source Converters With LCL Filters: A Study Based on Different State Feedbacks," *IEEE Trans. Power Electron.*, vol. 31, no. 7, pp. 5189-5200, July 2016.

[29] P. Cortes et al., "Guidelines for weighting factors design in Model Predictive Control of power converters and drives," *2009 IEEE International Conference on Industrial Technology*, Gippsland, VIC, 2009, pp. 1-7.

[30] M. Malinowski, M. P. Kazmierkowski, S. Hansen, F. Blaabjerg and G. D. Marques, "Virtual-flux-based direct power control of three-phase PWM rectifiers," *IEEE Trans. Ind. Appl.*, vol. 37, no. 4, pp. 1019-1027, July-Aug. 2001.

[31] P. Rodríguez, A. Luna, R. S. Muñoz-Aguilar, I. Etxeberria-Otadui, R. Teodorescu and F. Blaabjerg, "A Stationary Reference Frame Grid Synchronization System for Three-Phase Grid-Connected Power Converters Under Adverse Grid Conditions," *IEEE Trans. Power Electron.*, vol. 27, no. 1, pp. 99-112, Jan. 2012.

[32] K. Ma, W. Chen, M. Liserre and F. Blaabjerg, "Power Controllability of a Three-Phase Converter With an Unbalanced AC Source," *IEEE Trans. Power Electron.*, vol. 30, no. 3, pp. 1591-1604, March 2015.

[33] Z. Ma, X. Zhang, J. Huang and B. Zhao, "Stability-Constraining-Dichotomy-Solution-Based Model Predictive Control to Improve the Stability of Power Conversion System in the MEA," *IEEE Trans. Ind. Electron.*, vol. 66, no. 7, pp. 5696-5706, July 2019.

Xiaotao Chen was born in Jiangshan, Zhejiang Province, China, in 1994. He received the B.S. degree in electrical engineering from Shanghai Maritime University, Shanghai, China, in 2017, where he is currently working toward the M.S. degree in electrical engineering.

His current research interests include digital control techniques of power converters.
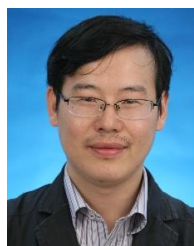
Weimin Wu received Ph.D. degrees in Electrical Engineering from the College of Electrical Engineering, Zhejiang University, Hangzhou, China, in 2005.

He worked as a research engineer in the Delta Power Electronic Center (DPEC), Shanghai, from July, 2005 to June, 2006. Since July, 2006, he has been a Faculty Member at Shanghai Maritime University, where he is currently a Full Professor in Department of Electrical Engineering. He was a Visiting Professor in the Center for Power Electronics Systems (CPES), Virginia Polytechnic Institute and State University, Blacksburg, USA, from Sept. 2008 to March. 2009. From Nov. 2011 to Jan. 2014, he was also a visiting professor in the Department of Energy Technology, Aalborg University, Demark, working at the Center of Reliable Power Electronics (CORPE). He has coauthored over 100 papers and holds eight patents. His areas of interests include power converters for renewable energy systems, power quality, smart grid, and energy storage technology. Dr. Wu serves as an Associate Editor for the IEEE TRANSACTIONS ON INDUSTRYELECTRONICS.

Ning Gao was born in Haining, Zhejiang Province, China, in 1987. He received the B.S. degree in electronics and information engineering from Zhejiang University, Hangzhou, China, in 2009, and the M.S. and Ph.D. degrees from Shanghai Jiao Tong University, Shanghai, China, in 2011 and 2017, respectively. Since 2017, he has been with the Department of Electrical Engineering, Shanghai Maritime University, Shanghai, where he is currently a lecturer.

His current research interests mainly include power converters applied in battery energy storage systems.

Henry Shu-Hung Chung (M'95–SM'03–F'16) received the B.Eng. and Ph.D. degrees in electrical engineering from The Hong Kong Polytechnic University, Hong Kong, in 1991 and 1994, respectively.

Since 1995, he has been with the City University of Hong Kong, Kowloon, Hong Kong, where he is currently a Professor in the Department of Electronic Engineering, and the Director of the Centre for Smart Energy

Conversion and Utilization Research. He has edited one book, and authored eight research book chapters, and more than 390 technical papers including 180 refereed journal papers in his research areas, and holds 40 patents. His research interests include time- and frequency-domain analysis of power electronic circuits, switched-capacitor-based converters, random-switching techniques, control methods, digital audio amplifiers, soft-switching converters, and electronic ballast design.

Prof. Chung is currently the Editor-in-Chief of the IEEE POWER ELECTRONICS LETTERS, and an Associate Editor for the IEEE TRANSACTIONS ON POWER ELECTRONICS and the IEEE JOURNAL OF EMERGING AND SELECTED TOPICS IN POWER ELECTRONICS.

Marco Liserre (S'00-M'02-SM'07-F'13) received the MSc and PhD degree in Electrical Engineering from the Bari Polytechnic, respectively in 1998 and 2002. He has been Associate Professor at Bari Polytechnic and from 2012 Professor in reliable power electronics at Aalborg University (Denmark). From 2013 he is Full Professor and he holds the Chair of Power Electronics at Kiel University (Germany). He has published 400 technical papers (more than 1/3 of them in international peer-reviewed journals) and a book. These works have received more than 28000 citations. Marco Liserre is listed in ISI Thomson report "The world's most influential scientific minds" from 2014.

He has been awarded with an ERC Consolidator Grant for the project "The Highly Efficient And Reliable smart Transformer (HEART), a new Heart for the Electric Distribution System".

He is member of IAS, PELS, PES and IES. He has been serving all these societies in different capacities. He has received the IES 2009 Early Career Award, the IES 2011 Anthony J. Hornfeck Service Award, the 2014 Dr. Bimal Bose Energy Systems Award, the 2011 Industrial Electronics Magazine best paper award and the Third Prize paper award by the Industrial Power Converter Committee at ECCE 2012, 2012, 2017 IEEE PELS Sustainable Energy Systems Technical Achievement Award and the 2018 IEEE-IES Mittelmann Achievement Award.

Frede Blaabjerg (S'86–M'88–SM'97–F'03) was with ABB-Scandia, Randers, Denmark, from 1987 to 1988. From 1988 to 1992, he was a Ph.D. Student in Electrical Engineering with Aalborg University, Aalborg, Denmark. He became an Assistant Professor in 1992, an Associate Professor in 1996, and a Full Professor of power electronics and drives in 1998. From 2017 he became a Villum Investigator.

His current research interests include power electronics and its applications such as in wind turbines, PV systems, reliability, harmonics and adjustable speed drives. He has published more than 450 journal papers in the fields of power electronics and its applications. He is the co-author of two monographs and editor of 6 books in power electronics and its applications. He was the Editor-in-Chief of the IEEE TRANSACTIONS ON POWER ELECTRONICS from 2006 to 2012.